In vivo subcellular resolution optical imaging in the lung reveals early metastatic proliferation and motility

David Entenberg[1,2,3,†], Carolina Rodriguez-Tirado[4,†], Yu Kato[4,†], Takanori Kitamura[4,5], Jeffrey W Pollard[4,5,*], and John Condeelis[1,2,3,*]

[1]Department of Anatomy and Structural Biology; Albert Einstein College of Medicine; Bronx, NY USA; [2]Gruss Lipper Biophotonics Center; Albert Einstein College of Medicine; Bronx, NY USA; [3]Integrated Imaging Program; Albert Einstein College of Medicine; Bronx, NY USA; [4]Department of Developmental and Molecular Biology and the Department of Obstetrics/Gynecology and Woman's Health; Albert Einstein College of Medicine; Bronx, NY, USA; [5]Medical Research Council Centre for Reproductive Health; Queen's Medical Research Institute; University of Edinburgh; Edinburgh, UK

[†]These authors contributed equally to this work.

To better understand breast cancer metastatic cell seeding, we have employed multiphoton microscopy and a vacuum stabilized window which eliminates the need for complex registration software, video rate microscopy or specialized gating electronics to observe the initial steps of tumor cell seeding within the living, breathing lung. We observe that upon arrival to the lung, tumor cells are found exclusively in capillary vessels, completely fill their volume and display an initial high level of protrusive activity that dramatically reduces over time. Further, we observe a concomitant increase in positional stability during this same period. We employ several techniques accessible to most imaging labs for optimizing signal to noise and resolution which enable us to report the first direct observation, with subcellular resolution, of the arrival, proliferation, and motility of metastatic tumor cells within the lung.

Introduction

Cancer is the second leading cause of death within the US with 90% of mortality due to metastases.[1] Of the 3 major sites of breast cancer metastasis observed clinically (bone 78%, lung 35% and liver 20%[2]), the most difficult to access for *in vivo, intravital* optical imaging is the lung, a vital organ enclosed within the thoracic cavity and undergoing perpetual motion. This inaccessibility of the lung to high-resolution optical imaging modalities has led cancer growth at this site to be called "an occult process".[3]

Since Malpighi's first observations of the excised lung in 1664,[4] this organ has been recognized as unique within the body. Its membranous nature makes it particularly susceptible to damage and artifacts, making intact imaging both desirous and difficult to achieve. In the clinical setting, standard imaging modalities for diagnosis and treatment of the lungs include PET, MRI and CT. While these technologies provide clinicians a direct view into this otherwise inaccessible organ, their low resolution limits their use to gross pathology since the smallest metastases detectable already consist of thousands of cells. Observation of the earliest metastatic seeding events and their dynamics is impossible with these modalities and instead requires direct observation by optical microscopy.

The use of high resolution *in vivo* optical imaging within the primary tumor has proven to be crucial to understanding the metastatic cascade, allowing direct quantification of single-cell and sub-cellular parameters (e.g. directional migration, turning frequency and persistence, velocity, protrusiveness, type of protrusion, etc.), as well as interactions between tumor cells and host cells. For example, high resolution imaging of tumor cell protrusions and invadopodia has led to the discovery of discrete microenvironments supportive of either growth or invasion within the primary tumor[5] as well as the preferential role of streaming in intravasation.[6] Finally, high resolution imaging is critical for understanding tumor cell behavior in lung due to the fine structure of the capillary bed.

Unfortunately, in the lung high resolution technologies have traditionally only been able to image fixed, sectioned tissues, or at best, ex vivo whole mount explants.[7,8] In either case, the cellular dynamics and interactions are lost and the perfusion of capillaries and oxygenation of cells is altered.

While in the minority, several groups have been successful at imaging the intact living lung. Wearn and German[9] were the first to accomplish this by surgically removing the outer chest wall down to the pleural layer and imaging through this layer with a microscope. This was followed by Terry in 1939[10] who was the first to utilize an implanted optical window. This window utilized an "exhaust tube" to apply vacuum, removing air from the thoracic cavity and drawing the tissue to the window. Since that time, a variety of optical windows have been developed.[11-19]

Of course, a major impediment to microscopic evaluation of the lung tissue is the fact that the lungs are in constant motion. To address this limitation, Wagner and Filley in 1965 attempted to locate their implanted window over a relatively stationary region of the canine lung.[12] This surgery however was quite traumatic and involved the complete resection of the forelimb. In 1967, Wagner employed vacuum explicitly to stabilize the motion of the lung tissue. Since that time, a number of groups have employed vacuum to stabilize the constant motion of the lung[10,13,14,16,18,19] with Lamm and Glenny[16] reducing the size of their window to employ in rats and Looney and Krummel[18] further miniaturizing their window for use in mice. Finally Presson and Petrache employed a fixturing plate to further reduce the motion artifacts and attain full tissue immobilization at the microscopic level eliminating the need for electronic gating and in most cases post processing software as well.[19] In this scheme, the vacuum window stabilizes the tissue and the stage plate stabilizes the window removing the residual motion of the window. The success of these vacuum stabilized imaging windows has even recently been extended to imaging the beating heart.[20]

Although these vacuum based window technologies have allowed imaging into the lung, the prior reported systems have focused either on pulmonary dynamics or on the surveillance of the lung by immune cells.[16,19] The requirements for these studies are different than for imaging cancer growth and motility where subcellular resolution is required to image cell division, organelle content, protrusion and cellular dynamics[5] rather than large fields of view used to capture cells with high velocities.

In this technical report, we present a unique combination of several technologies designed to attain the highest resolution intravital images possible of the living breathing murine lung. Our report combines an existing vacuum stabilized lung window designed to completely immobilize the lung tissue with a unique combination of existing and novel signal optimization techniques that make possible the acquisition of some of the first high resolution, subcellular intravital images of tumor cell arrival, proliferation and motility within the lung. In particular, the blood averaging technique presented yields an unprecedented clear view of the lung microvasculature *in vivo* which has the power to distinguish between active attachment and physical lodging of tumor cells in the capillary bed while the PMT amplifier optimization yields an approximate 20-fold improvement in signal to noise that allows visualization of fluorophore exclusion from the nucleus and the visualization of chromosomal separation during mitosis. Taken together, the novel combination of these intravital imaging advances (both newly conceived and existing), make

feasible detailed quantitative analyses of sub cellular structures in the *in vivo* lung not previously possible.

Results

Window design & implementation

The miniature vacuum-stabilized imaging window employed in this work is similar in design to that published by Presson et al.[19]. We chose this window as a starting point because, as discussed below, the superior tissue fixturing that this design provides enables stable imaging without the requirement for either video rate imaging equipment or electronic gating of acquisition to eliminate respiratory motion. In our design (shown in **Fig. 1**), the window, made of Teflon, consists of a battlement topped wall separating a 4.4 mm diameter inner chamber from an 8.7 mm diameter outer chamber. Vacuum applied to the outer chamber via a circular port (lower left corner of **Fig. 1A**) on the outside wall is conveyed by the battlements to the inner chamber. When the window is in place, the lung tissue is drawn outwards to touch the 10 mm glass coverslip that sits inside of the recessed rim and rests upon the battlements. To make an air tight seal, the coverslip is adhered to the rim with cyanoacrylate glue. The reverse side (not shown) is smooth and tapered to conform to the shape of the lung.

Presson et al. reported that in their hands the window occasionally did not work, and as a result, they developed a computational motion compensation algorithm to be applied post acquisition when needed. Our initial experience with the imaging window was similar to that reported by Presson et al. where complete stabilization of the tissue was not always achieved. However with experience, we determined that the major cause of this failure was due to a breach of the vacuum seal due to placement of the lung tissue off center of the window inner chamber. When careful centration was maintained, failure was virtually eliminated.

Since vacuum stabilized windows necessarily breach the seal of the thoracic cavity to access the lung tissue, forced ventilation is required. This involves either intubating the mouse with a tracheal catheter or performing a tracheotomy (**Fig. 1C**). We have observed that the intubation method proves to be less traumatic for the mouse and consistently leads to longer survival times: extended from <5 hours to 12 hours (limited only by IACUC protocol).

Ventilation is then followed by exposing the lung tissue by surgical excision of several ribs (**Fig. 1D**) and finally attachment of the window to the lung. While this window design is similar to many of the prior reported windows, the key advancement of the Presson et al. design lies in its combination with a fixturing plate (**Fig. 1B**) for use on an inverted microscope.

The efficacy of the fixturing plate can be seen by understanding the types of motion the lung tissue undergoes. The combination of forced ventilation with the mouse's own natural attempts at respiration causes 2 different types of motion of the lung which must both be stabilized. **Supplemental Movie 1** shows the effects of these 2 motions without stabilization. The forced ventilation causes the rhythmic, shaking of the field of view with excursions of less than one field of view that occur at the ventilation rate
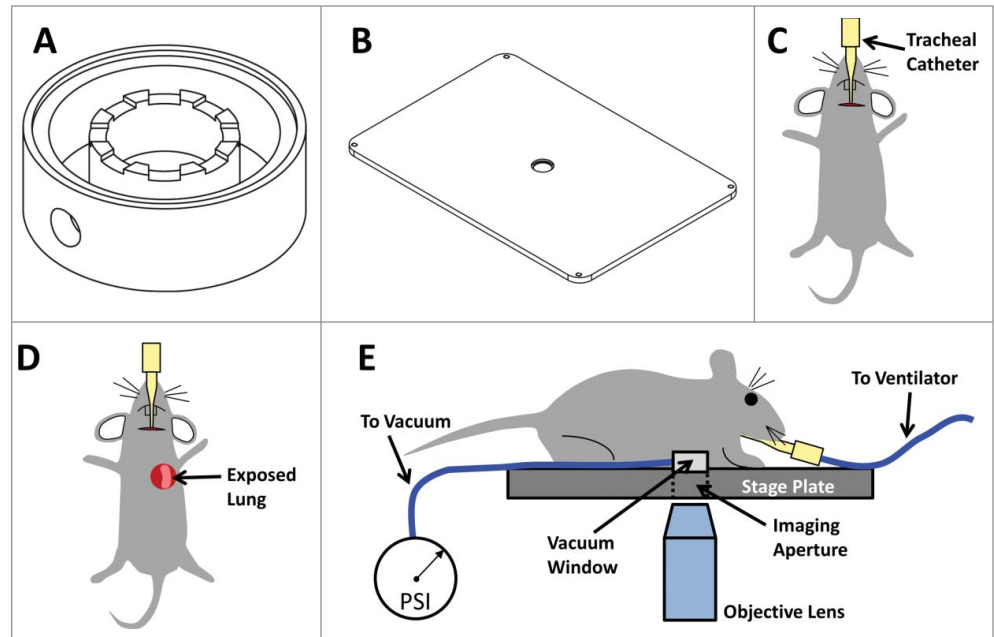
(120bpm). The mouse's attempts at natural respiration however cause a large-scale contraction of the intercostal muscles and are much larger in extent, to the point that without the vacuum stabilization, the tissue separates from the coverslip, manifesting as a black band in the image. Since the natural breath rate of ~60 breaths per minute was very close to (but not synchronized with) the frame acquisition rate of 1 frame per second (FPS), the black band appears to scroll across the field of view.

The operating principle of vacuum window designs is to draw the lung tissue through the central chamber to touch the coverslip and stabilize the smaller motions due to forced-ventilation. The presence of the fixturing plate acts in combination with this vacuum stabilization to further remove the natural respiration motion. The effect of this can be seen in **Supplemental Movie 2** that shows another field of view, this time with the vacuum stabilization and fixturing plate applied. As is evidenced by the stationary collagen fibers (dark blue), complete stabilization of the image is achieved.

Figure 1. Lung Imaging Window: The Lung Imaging Window utilizes vacuum to attach the lung tissue to the coverglass, thereby immobilizing the tissue, and fixtures the window within a stage plate, thereby immobilizing the window. This new design prevents motion artifacts and eliminates the need for either timing image acquisition with breathing/ventilation or complex image registration algorithms. **(A)** Computer Aided Design (CAD) drawing of Lung Imaging Window. **(B)** CAD drawing of fixturing stage plate. The center hole which serves as an imaging aperture through which the objective lens images the lung tissue, has a tightly toleranced step which accepts the imaging window. **(C–E)** Cartoons showing the steps of the lung window surgery. **(C)** An incision in the neck through the skin and salivary gland allows access to the trachea for insertion of a catheter which is connected to a ventilator. **(D)** With the catheter in place, the skin, muscle and ribs are removed exposing the left lung. **(E)** The vacuum window is attached to the stage plate and connected to the vacuum line. The mouse is inverted and positioned so the exposed lung tissue is covers the window. The vacuum is then turned on and imaging may be performed through the imaging aperture.

Use of proper vacuum levels is critical to both maintaining the imaging field stability and the structural integrity of the lung tissue. Too little vacuum is inadequate for field stabilization, while too much vacuum results in compressed blood vessels, disrupted perfusion and capillary damage. In our setup we have found that once the correct level has been determined, the setting is consistent across all experiments and does not require further adjustment. As a method of verification of the vacuum level, we only introduce the vascular label (intravenous injection of fluorescent dextran) after the surgery is complete and the vacuum has been applied to the lung. This arrangement ensures that only properly perfused and healthy vasculature becomes labeled and lung tissue that may have been inadvertently damaged during surgery can be identified by the presence of dextran in the extravascular space.

Resolution and signal optimization

The novel aspect of our work here is the combination of this vacuum stabilized imaging window with a multiphoton microscope optimized for signal to noise and resolution. This combination opens the technique up to the multitude of laboratories with point scanning microscopes and removes the requirement for complex registration software, video rate microscopes or specialized gating electronics.

As mentioned in the introduction, other high resolution imaging studies[5,21] have demonstrated the necessity of utilizing high resolution imaging in the primary tumor. This is especially true for imaging lung tissue due to the fine structures of the capillary bed. Here the attainment of subcellular resolution is accomplished by the optimization of resolution and signal to noise on several different fronts. Firstly, multiphoton signal generation is dependent upon maintaining the smallest focal volume possible for the illumination beam. This means that the focal spot within a laser scanning microscope must be limited in lateral as well as axial spatial extents.[22]

Objective lens selection

The lateral extent of the focus (and hence the ultimate resolution of the microscope) is directly controlled by both the numerical aperture of the objective lens and its aberrations.[23] To this end, we have employed an objective lens specifically engineered for 2-photon applications (XLPL25XWMP Olympus). This lens provides several advantages including a >82% transmittance over the visible and near infrared (NIR) range, one of the highest Numerical Apertures (1.05) available for a long working distance (2 mm) water immersion lens and chromatic correction specifically for green, red and infrared wavelengths. This last point is

crucial to attaining optimal performance within a multiphoton application as it is the NIR illumination beam which generates the visible-wavelength 2-photon signal. As this signal needs only to be collected and not imaged through a pinhole (as in the case of confocal microscopy), control of aberrations for the emission wavelengths is not crucial. As a demonstration of the performance of this choice of objective lens, we have measured the point spread function of the 25x 1.05NA objective mentioned above. As can be seen in **Figure S1**, our measured point spread function compares well with the theoretical limits of 322 nm and 1,073 nm in the lateral and axial directions respectively.

GVD compensation

While the axial extent of the focal volume is also controlled by the numerical aperture of the lens, a larger impact on the signal generated is that of the temporal width of the pulsed laser. Typical commercially available femtosecond pulsed lasers generate light pulses in the NIR with an extent of ~90–100fs, ideally suited for multiphoton applications. Unfortunately, pulses within this range experience significant levels of dispersion: the shorter the pulse, the more the dispersion (see Newport Application Note 29 https://www.newport.com/Application-Notes/981012/1033/content.aspx). Broadening of these pulses can lead to significant degradation of mulitphoton fluorescence levels.[24] In our system we have employed a double pass group velocity dispersion (GVD) compensation system[24,25] which effectively triples the fluorescence signal generated.

Choice of PMT amplifier

Once the fluorescence signals have been generated, detection must be performed in a way which preserves the signal to noise ratio to the greatest degree. Photo-multiplier tubes (PMTs) are the detector of choice for multiphoton applications due to their high linearity, large detector area, exceptionally fast response time and high internal gain. This last point makes PMTs particularly useful for weaker signals, despite their relatively low quantum efficiency. While the utility of PMTs for low signal levels is widely recognized, the fact that the noise level of a PMT is also dependent upon the gain is not. In fact, as a PMT is driven near its maximum of gain, its noise level dramatically increases. This can be seen in **Figure S2A and S2B** where the output of the PMT was measured as a function of its gain. Thus, optimization of signal to noise in an imaging system relies upon operating with as high of a laser power as possible without damaging the sample and as low of a PMT gain setting as possible while still generating an appreciable signal. One factor that determines at how low of a gain at which a PMT may be operated is the trans-impedance amplifier to which it is connected.

Since all PMTs generate signal in the form of a flow of electricity (usually on the order of pico- to micro-Amperes) a transimpedance amplifier must be employed to convert this current into a measurable and buffered voltage. In all amplifiers, there is a trade-off between amplification and speed: the higher the bandwidth, the lower the overall amplification,[26] however, this is particularly pronounced in trans-impedance amplifiers used with photodetectors due to latter's high capacitance.[27]

In our previously reported system design, we had chosen a trans-impedance amplifier (HC130–03, Hamamatsu) which simultaneously optimized gain and bandwidth for acquisition of images acquired with a pixel clock speed of ~1MHz. In our microscope, this was driven by the need to acquire 1024×1024 images at 1 frame per second (fps). However, in an attempt to maximize the signal to noise of our system, we opted in this work to employ a different, slower amplifier with a significantly higher gain (C7913, Hamamatsu). This required relaxing the bandwidth requirement on the amplifier and limits our acquisition to 512 × 512 pixel images at 1 fps or 1024 × 1024 pixel images at 0.25 fps. The significantly higher gain factor (C7913 = 10,000,000 V/A vs. HC130–03 = 3,000 V/A) with similar noise specifications (C7913 = 2 mV RMS vs HC130–03 = 3 mV RMS) allows the PMT to operate at a markedly lower gain setting (C7913 = 52% vs HC130–03 = 90%) and reduces the noise by a factor of 10 to 20 under normal *in vivo* imaging conditions.

As a test of this, we took advantage of the adjustable gain setting available on the C7319 amplifier which allows selection of 10^5, 10^6 or 10^7 V/A and directly compared the signal to noise ratio generated by 8 μm fluorescent beads using each of these settings as well as the H130–03 amplifier (**Fig. S2C**). For these measurements, all imaging parameters were kept constant except for the PMT gain and the amplifier setting which were adjusted so as to generate approximately the same signal level from the beads. As can be seen, signal to noise increases with increasing post amplification gain and the C7319 operating at its highest gain setting results in a significantly improved signal to noise over the HC130-03 amplifier.

Figure S2D conveys the advantage this amplifier gives by showing an image of a sample of crystalized Tracker Red dye imaged with the same PMT under the same illumination and scan parameters but with different amplifiers and the PMT adjusted to produce roughly the same post amplifier output signal: in the case of the HC130–03, the PMT gain was required to be 90%, while the C7913 remained at 52%. As can be seen, the C7913 showed marked improvement in salt-and-pepper noise, overall background, image graininess and SNR (4.3 vs. 26.2).

Point averaging

Once the signals have been collected, limitations on galvanometer scan speeds imposed by the inertia of the mirrors offer an additional opportunity for signal to noise improvement. As described previously,[24] our system employs acquisition electronics with bandwidths several times higher than the pixel acquisition rate. By running the acquisition electronics at a higher clock rate than the pixel clock, several samples may be acquired per pixel. Averaging these pixels together enables dramatic reductions in residual salt-and-pepper noise and background levels without any sacrifice of acquisition speed.[24]

Blood averaging

Finally, the superior image stability attained with our vacuum window setup enables a dramatic increase in the signal from stationary structures by averaging them over time. In the case of the
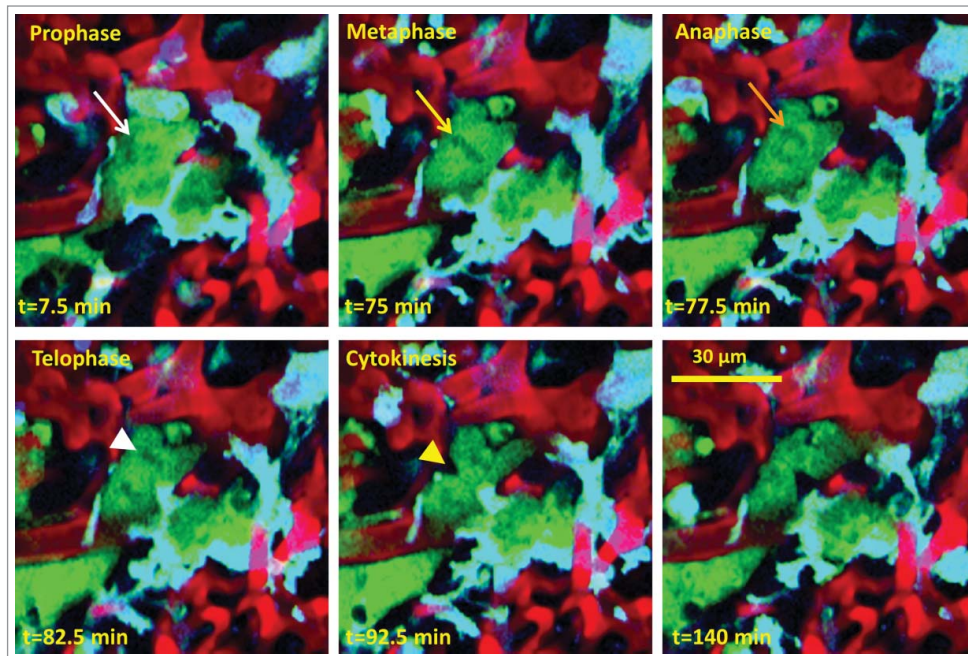
lung window, this is particulary useful as the morphology and structure of the vasculature does not vary over the time period of the experiment (5–12 hrs). As shown in **Supplemental Movie 3**, the passage of the unlabled erythrocytes and monocytes through the narrow dextran filled capillaries causes a flashing which obscures the vessel boundaries as the dextran is excluded. The situation is exacerbated by the presence of tumor cells or macrophages which can temporarily block the flow of blood completely. This obscures the vessel and makes determination of the vessel boundary difficult. As a demonstration of the level of this signal variation, **Figure S3A** shows a still from this movie with 2 regions of interest demarking intravascular space. **Figure S3B** shows the same field of view and regions of interest time averaged. Signal from region 1 and region 2 was directly measured and plotted in panel C (left = Roi 1 and right = Roi 2) which shows a variation in signal from 100 to <20% of maximum. Averaging over time for the blood vessel channel completely removes this flashing and clearly defines the vessel boundaries (**Figure S3B** and **Supplemental Movie 4**).

Figure 2. Stable imaging with sub-cellular resolution of the intact, breathing lung. Still images from a 140 min long time lapse movie showing a micro-metastasis in the lung 5 d after single tumor cells were introduced into the mouse via tail vein injection. In one cell, the unlabeled nucleus (arrows) appears as a shadow within the GFP labeled cytoplasm and reveals the cell progressing through the different stages of mitosis. The telophase stage is marked by the separation of pinching and separation of the cytoplasm of the 2 daughter cells (arrow heads). The red channel (blood labeled with 155kD Rhodamine-dextran) has been averaged over the duration of the movie and overlaid with the green (GFP tumor cells) and cyan (CFP macrophages) channels. Frames were acquired every 2.5 min with 3 frame averages per acquisition.

Tumor cell – immune cell interactions

To demonstrate the capability for subcellular resolution in our system, we performed intravital imaging of experimental lung metastases in MacBlue mice,[28] which express CFP in myeloid cells. Marking of the vasculature was accomplished by an intravenous injection of high molecular weight fluorescently labeled dextran, and the tumor cells were transfected to express the fluorescent protein Clover.[29]

Supplemental Movie 5 shows an example of the type of high-resolution imaging capable with the optimizations described in this manuscript. In this single slice from a 4D movie taken 24hrs after tail vein injection, 2 macrophages are seen stably interacting with a tumor cell. While the tumor cell is observed to undergo only small protrusions, the macrophages extend extremely long, thin pseudopods that would not be visible at lower resolution. A 3D reconstruction of this data is presented in **Supplemental Movie 6**. This 3D reconstruction additionally shows that the stabilization is not only attained in the lateral xy direction, but also over the depth of imaging as well. For this data, z-stacks were acquired at a frame rate of ∼2 fps with 3 averages per frame. Each z-stack thus took ∼40 seconds to acquire. With a ventilation rate of ∼1–2 breaths per second, significant vertical sample motion would manifest as a blurring of the fine pseudopod extensions and would prevent clear 3D reconstruction. Thus these movements are not occurring.

Like others who have imaged in the lung, we have been able to acquire signal relatively deep (∼125 μm) into the lung tissue.[30] However, the many interfaces present in the lung rapidly aberrate the point spread function, and very high resolution images are only able to be acquired over a depth of approximately 50–60 μm.

Visualization of tumor proliferation

A further example of the detail that would remain hidden without these optimizations is shown in **Figure 2**. Here, one cancer cell is observed to undergo mitosis within a tumor cluster developed at 5 d after injection. At 7.5 minutes after the start of imaging, the nuclear condensation (white arrow) of prophase can be clearly seen. This continued until 75 minutes when a clear metaphase plate formed (yellow arrow). This was followed in quick succession by complete separation of the chromosomes in anaphase (orange arrow). Finally, telophase (white arrow head) and cytokinesis (yellow arrow head) occurred between 92.5 and 140 minutes. The complete progression of the mitotic process in a metastatic cancer cell can be seen in **Supplemental Movie 7**.

Dynamics of tumor cells in lungs

To show the power of this optical imaging setup, we imaged the lung immediately (as well as 12 and 24hrs) after tumor cell

injection via the tail vein. In our setup, we could easily image the arrival of circulating tumor cells to the lung. We observed that tumor cells are found exclusively in capillary vessels smaller than the diameter of a tumor cell ($\sim$20μm see **Fig. 3D**), and remain in this size of vessels until extravasation which occurs between 24 and 36 hours. Further, these cells completely fill the capillary lumen to the point of exclusion all dextran from the capillary volume: no leakage can be observed between the cell boundary and the vessel wall.

In order to quantify this observation, we analyzed the average dextran signal within 80μm^2 circles located either on top of the cell, within the extravascular space or within the vessel lumen (**Fig. 3A**). **Figure 3A** shows stills taken from one example 2hr movie (**Supplemental Movie 8**) both with the tumor cell channel included (top row, green) and turned off (bottom row) to reveal the colocalizing dextran signal (red). **Figure 3B** demonstrates a representative quantification of the time course of the dextran signals within the 3 locations indicated. These tumor signals were then averaged for 5 cells in 3 different mice and compared.

As shown in **Figure 3C**, no statistical difference was observed between the dextran levels measured within the tumor cell

volume and the extravascular space while the level of dextran within the flowing vessels averaged $\sim$20 times greater. As an alternative analysis showing that these cells are physically lodged in the vasculature, we measured the diameter of the vessels containing tumor cells immediately after tail vein injection. The histogram in **Figure 3D** shows the diameter of 50 tumor cell containing vessels measured in 5 different mice. All of the cells were contained in vessels smaller than a single cell diameter ($\sim$20 μm).

We further observed that immediately upon arrival to the capillary bed in the lungs, cells transiently display a highly protrusive phenotype (**Supplementary Movie 9**) with processes that extend down, and retract from, capillary side branches. This phenotype persists with reduced magnitude at 12 hrs and is practically absent by 24 hrs (**Supplementary Movies 10 and 11**). This is most easily observed by viewing the cell border outlines from each time point overlaid in a single image (**Fig. 4A**). As discussed in the Materials and Methods section, we quantified the cell area and the standard deviation of the area difference between each time point.

While comparison of the mean cell area between the 3 time points fails to show a statistical difference (**Fig. 4B**, top), a direct analysis of just the protrusions shows a statistically significant reduction between 0 and 12 hrs as well as between 0 and 24hrs (**Fig. 4B**, bottom) indicating larger protrusions at 0 hr. No statistical difference is observed between 12 and 24 hrs.

We also analyzed the cell average instantaneous velocity (speed) and its jitter as measured by the standard deviation. We found a significant reduction in average cell speed (centroid translocation) between 0 and 24 hrs (**Fig. 4C**, top) along with a concomitant reduction in the standard deviation of the speed between the same time points (**Fig. 4C**, bottom), indicating a stabilization in cell position.
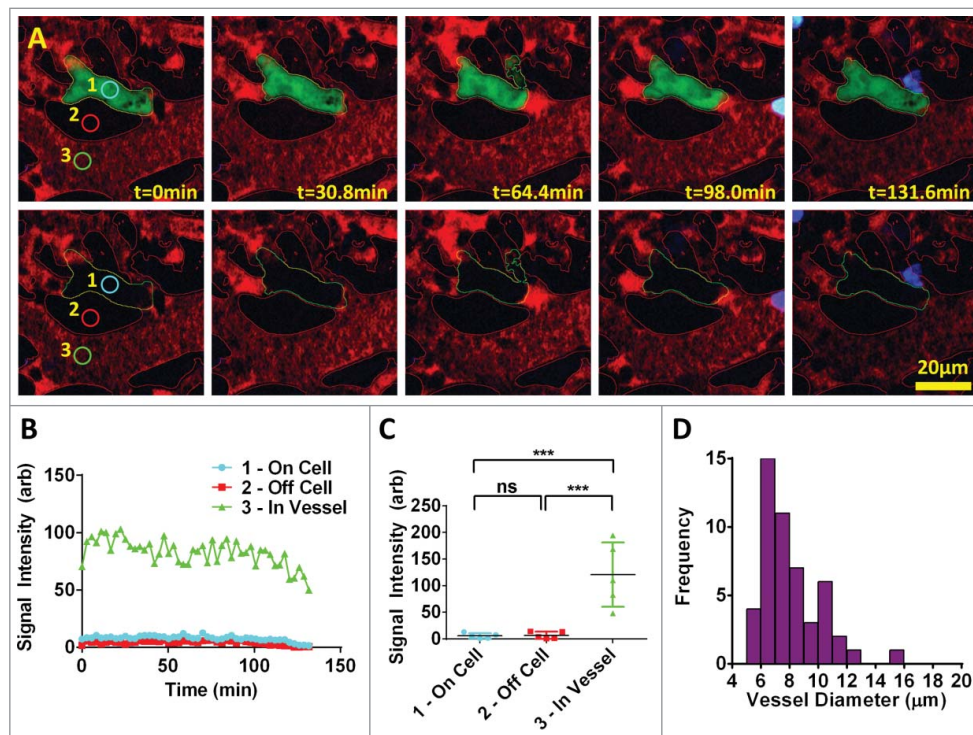
Figure 3. Tumor cells lodge in capillaries and completely fill their lumen immediately after tail vein injection. **(A)** Stills taken from a time lapse movie showing a tumor cell lodged in a capillary immediately after tail vein injection. Dextran signal was quantified within 80μm^2 circles in 3 locations: 1 – on top of the tumor cell, 2 – in the extravascular space and 3 – in the lumen of a flowing vessel. Cyan = macrophages, Green = Tumor cells, Red = Dextran. **(B)** Quantification of the time course of the dextran signals within the 3 locations indicated in **A**). **(C)** Analysis of the dextran exclusion observed in movies of 5 cells within the lungs of 3 different mice. No statistical difference was observed between the dextran levels measured within the tumor cell volume and the extravascular space while the level of dextran within the flowing vessels averaged 20 times greater. Error bars: SEM, n=5 from 3 mice, *** = p<.0001. **(D)** Histogram of the diameter of vessels containing tumor cells immediately after tail vein injection. All of the vessels (50 cells in 5 mice) were under the single cell diameter of $\sim$20 μm

Discussion

We have developed a system that is capable of imaging the living breathing lung using high resolution multiphoton microscopy.

By combining a previously published vacuum stabilized imaging window[19] with a custom built 2-laser multiphoton microscope[24] specifically designed to optimize

resolution and signal to noise, we have attained complete tissue immobilization and exceptional subcellular resolution imaging of experimentally metastasized tumor cells.

Using this system, we have accomplished what is, to our knowledge, the first direct observation, with subcellular resolution, of the arrival, growth (cell division) and motility of metastatic tumor cells in the living, breathing lung.

We utilize a high NA (1.05) IR corrected objective lens for optimal point spread function, a GVD compensator to optimize the signal generated and a high gain amplifier which allows the PMTs to be run at a lower gain reducing the detector signal to noise.

Our design attains enough stabilization of the tissue to allow clear observation of chromosomal separation during mitosis, without any complex image registration algorithms or requiring specialized electronics to perform gated acquisitions timed with breathing/ventilation.
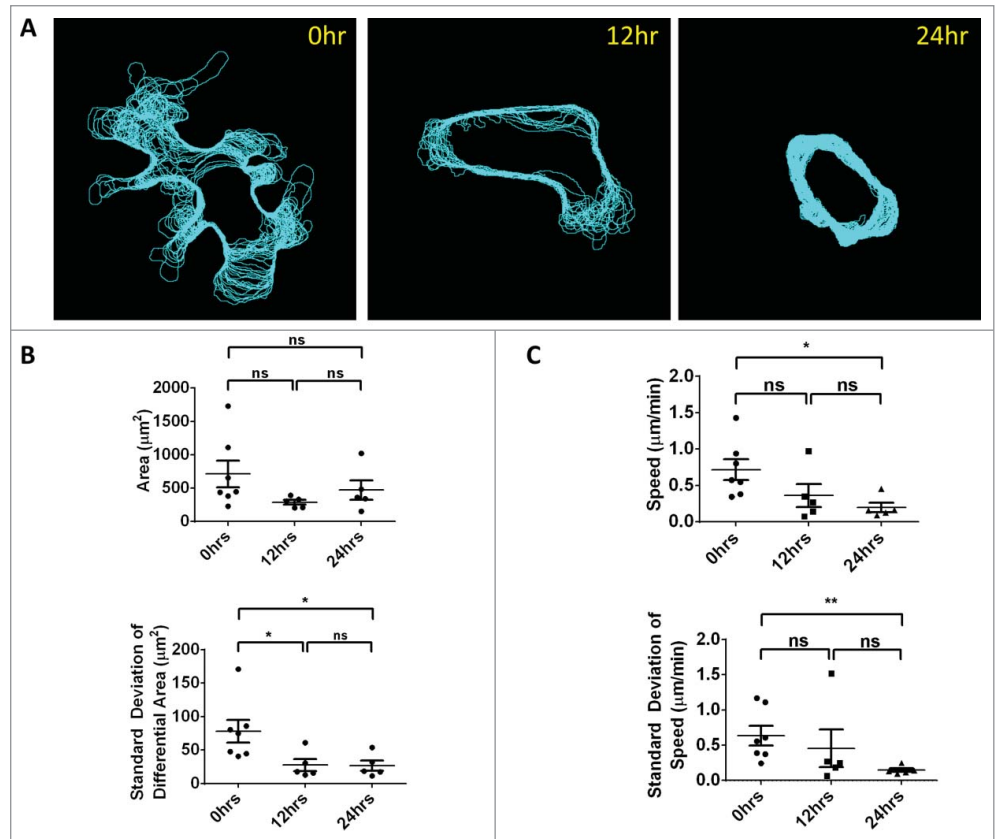
Further, the spatial stability of the time-lapse images acquired with this system allows for a dramatic improvement in signal to noise of stationary structures by averaging their signal over time. This is particularly important for imaging structures such as the lung

Figure 4. Quantification of motility and protrusions. Immediately after tail vein injection, tumor cells lodge in the vasculature of the lung, exhibit large protrusions and continue to slowly move down the length of the capillary. These protrusions decrease with time. **(A)** Outlines of cell boundary over the length of the movies overlaid on a single image. **(B)** Top: Quantification of mean cell area shows no statistically significant difference between 0, 12 and 24 hrs. Bottom: Quantification of the standard deviation of the area difference between each time point and the starting frame. Larger standard deviations in this differential area are indicative of larger protrusions and decrease significantly by 12 and 24 hrs. Error Bars = SEM. **(C)** Analysis of the cell average instantaneous velocity (speed) and its jitter (as measured by the standard deviation) show a significant reduction between 0 and 24 hrs indicating a stabilization in cell position. No difference is observed between 0 and 12 hrs and between 12 and 24 hrs. Top: Quantification of the cell centroid average instantaneous velocity. Bottom: Quantification of the standard deviation of the cell centroid speed. Error Bars = SEM.

capillary bed that are morphologically stationary, but have a fluctuating signal due to the passage of unlabeled erythrocytes and immune cells within their lumen.

Using this system, we have been able to image the early steps of tumor cell homing to the lungs as well as the beginnings of tumor cell-immune cell interactions with high enough resolution to perform quantitative analyses of the motility and membrane dynamics of the tumor cells in the vasculature.

Given the estimate that >80% of disseminated tumor cells that do make it to the lungs do not persist to form overt metastases,[31] understanding the mechanisms mediating tumor cell arrival and survival at secondary sites may result in novel therapies specifically targeting this step. Despite this importance, studies attempting to evaluate the fate and conditions of these cells have reported conflicting results. In particular, several studies have looked at whether arrival of disseminated tumor cells to secondary sites involves active adhesion of the cells to the endothelium or physical entrapment due to size restrictions.[32–35] Of these

studies, the ones by Al-Mehdi et al. and by Wong et al. (using whole mount lung explants) observed tumor cell arrest in vessels larger than the diameter of the cells, while intravital experiments (in the liver) by Morris et al. and Scherbarth et al. observed tumor cell entrapment in the capillary bed.

We observe that immediately upon arrival to the lungs, tumor cells are located solely in capillaries and completely fill their volume to the exclusion of blood serum (as indicated by IV- injected fluorescent dextran). This first direct observation of the arrival of tumor cells to the intact lung is suggestive of entrapment due to physical restraint of the cells rather than an active attachment. Further, the observed lack of a significant difference in cell area over the first 24 hrs indicates that neither cell division nor a significant amount of blebbing occurs during this initial time period. All of our direct observations of cell division have occurred at time points greater than 5 d (data not shown) where the cell numbers are greater and the probability of catching this relatively rare event is higher.

Immediately upon arrival, tumor cells are observed to exhibit a high-protrusion phenotype which reduces dramatically by 24 hrs along with a concomitant reduction in cell instantaneous velocity and jitter (as measured by the standard deviation of the centroid speed). Our high resolution imaging results suggest that the high-protrusion phenotype is a residue of a phenotype observed in the primary tumor where 2 distinct and mutually exclusive tumor cell phenotypes are observed, a fast migration-associated, locomotory protrusion phenotype; and a slow-loco-motion invasive protrusion phenotype associated with the presence of invadopodia and transendothelial migration.[5] The loss of locomotory protrusion activity from the tumor cells over time in the vasculature suggests that the locomotory protrusive phenotype is stimulated and maintained by the tumor microenvironment of the primary tumor but not by the microenvironment present in blood vessels.

Taken together, these data seem to indicate a model wherein cells arrive to the lungs, physically lodge and become trapped in the vasculature and subsequently undergo a transition from a protrusive and locomotory phenotype to a more invasive phenotype in preparation for crossing the endothelium. This interpretation is bolstered by previous measurements in ex vivo whole lung mounts which show that extravasation occurs between 24 and 48 hrs.[7]

More work needs to be done toward establishing the protease and integrin dependence of both the high and low protrusion phenotypes along with combination with markers of cell viability so as to distinguish those cells destined to survive and extravasate from those destined to die. Unlike the evidence for the involvement of invadopodia in intravasation[5,36,37] literature on extravasation has been so far controversial in terms of whether invadopodia are essential for cell crossing to occur and one of our near-future goals is to examine this.

In conclusion, our work demonstrates that imaging of early metastatic events is possible and opens the door for further studies aimed at elucidating the mechanisms behind metastatic seeding. This procedure will be useful to characterize the microenvironmental factors important to tumor cell survival, extravasation, dormancy and colonization of the secondary site. It also offers the opportunity to directly observe responses to chemotherapeutic agents

Methods and Materials

Here we report the development of a system capable of performing multiphoton imaging, with subcellular resolution, within the living breathing lung.

PMT noise measurements
For the PMT gain measurements, a CW diode laser (PhoxX 488–60, Omicron) was used to illuminate an autofluorescent plastic slide (Part #92001, Chroma) and the fluorescence recorded by the PMT (H7422P-MOD, Hamamatsu). The gain was set to the required value and the laser intensity varied so as to produce an appreciable signal within the linear operation region of the PMT. Calibrated absorptive neutral density filters (NEK01, Thorlabs) were employed to accurately reduce the laser intensity for the larger gain settings. The recorded PMT signal was then divided by the laser intensity to produce a power adjusted signal. Finally the signals were normalized to the maximum value to produce a percent signal.

For the amplifier comparison measurements, 5 μL of 8 μm fluorescent bead stock suspension (DG06M, Bangs Laboratories, Inc.) were placed in 1 mL of PBS in a MatTek dish and imaged using multiphoton excitation. All imaging parameters were kept constant except for the amplifier setting and the PMT gain which was adjusted to generate an approximately consistent signal level (~80% of gray level saturation). Images were analyzed with a custom ImageJ[38] macro which created a copy of the image, applied a 2 pixel median filter and thresholded just above background to segment the beads. The Analyze Particles function was then applied to outline the individual beads. These outlines were then applied to the original image and 10 individual beads measured to determine the average bead signal level. Finally, all of the ROIs were combined and the selection inverted so as to measure the background signal level.

Surgery
Surgical preparation proceeded according to a protocol similar to that presented by Presson and Petrache.[19] Briefly, 6–8 week old MacBlue mice B6;FVB-Tg(Csf1r-Gal4VP16/UAS-ECFP)$_{hume}$) were anesthetized with 1–5% isofluorane and an indwelling catheter inserted into the tail vein. Hair was removed from the chest and neck region with depilatory lotion.

Ventilation was accomplished either by intubation with a 1 inch/20 G catheter, or by tracheostomy. In the latter case, the trachea was exposed by a lateral incision to the neck followed by mechanical separation of the salivary glands and tracheal smooth muscle. A 1 inch/20 G catheter was then inserted through the tracheal wall. In either case, the catheter was then connected to a ventilator providing 200 μL of air at ~140 cps.

Next, the skin and muscle over a 10 mm diameter section of the upper left thorax was removed. A cautery pen was used to seal any blood vessels prior to severing. Finally, the exposed ribs were resected and the lung was exposed. Extreme care was taken not to touch the lung tissue with the instruments. The mouse was then inverted and positioned above the imaging window which has been placed on the fixturing plate. With the mouse in position (the lung tissue completely covering the window), vacuum was applied to the window.

Imaging
Imaging was performed on a custom built 2-laser 2-photon microscope described previously.[24] Briefly, mice were prepared according to the Surgery section above and maintained under anesthesia during imaging using 0.75–2.5% isofluorane. Once upon the vacuum fixturing plate, mice were kept at physiological temperature by way of a forced heated-air environmental control chamber.

After application of the vacuum, 155 kD TRITC dextran (T1287–500MG, Sigma) (to label the vasculature) and 10^6

fluorescent tumor cells (if not having been previously introduced at an earlier time point) were administered via the indwelling tail vein catheter along with approximately 50 μL of saline per hour to maintain hydration.

During imaging, mice were continuously ventilated and vital signs were monitored using a pulse oximeter (MouseOx, Starr LifeSciences).

4D (time-lapse / z-stack) images of 3 separate stage positions were acquired for 3 to 12 hours. Care was taken to limit the laser intensity to a maximum of ~22 mW as intensities above this value were observed to cause tissue damage after several hours of constant imaging. This damage was evident by leakage of dextran into the alveolar space followed by a shutdown of vessel blood flow and perfusion. No such damage was observed at the lower intensity even up to 12 hours of imaging (IACUC limitation).

Animals were euthanized at the end of the imaging session. All animals were used according to protocols that have been reviewed and approved by Einstein's Institutional Animal Care and Use Committee.

Point spread function measurements

Measurement of the point spread function was accomplished following a slight variation of a published protocol.[39] In brief, a 0.1 μm fluorescent microsphere sample (TetraSpeck, Molecular Probes) was prepared by diluting the stock suspension $1:10^4$ in dH20, sonicating for 20 minutes, and finally diluting 1:100 in PBS. Beads were allowed to settle for 20 minutes before imaging. Theoretical resolutions were computed for each objective lens following the formulae given in Zipfel et al. (including the conversion to FWHM measurements).[40] For 25x 1.05NA objective using water immersion, the lateral and axial resolutions are 322 and 1,073 nm respectively. The Nyquist condition determines that sampling should be performed at better than 161 and 537nm respectively. As such, imaging was performed using better than Nyquist conditions with 100nm xy sampling and 200nm z sampling. Ten beads were averaged and processed using the MetroloJ plugin (http://imagejdocu.tudor.lu/doku.php?id=plugin:analysis:metroloj:start) for ImageJ.[38]

Blood averaging

Time-lapse image data sets were processed using a custom macro developed within ImageJ.[38] This macro separated the time lapse movie into its separate color channels, averaged the red (blood) channel over time producing a single image of the vasculature. This single image was then duplicated for each frame in the time-lapse and the other channels overlaid on this red channel.

Other processing

Occasionally a small amount of lateral drift was observed in time lapse movies due to a slight off center placement of the lung tissue. In these cases application of the StackReg plugin[41] for ImageJ restored motion free images.

Preparation of tumor cells

EO771 medullary breast adenocarcinoma cells were obtained from Dr. E. Mihich (Rosewell Park Cancer Institute, NY) and was originally isolated from a spontaneous mammary tumor in C57BL/6 mice.[42] Highly metastatic tumor cells (EO771-LG) were derived from the parental cell line by subjecting the former one to repeated cycles of experimental metastasis assays.[43]

Both cell lines were maintained as monolayer in DMEM media (Invitrogen) supplemented with GlutaMAX™-I, 10% fetal bovine serum (FBS), 15 mM HEPES, 1mM sodium pyruvate, 100U/mL of penicillin, and 110 μg/mL of streptomycin, at 37C and 5% CO2.

To track tumor growth, EO771-LG cells were transfected with either EGFP or Clover (Addgene plasmid 40259)[29] expressing plasmid using standard protocols with Lipofectamine 2000 (Invitrogen).

Image analysis

The high resolution images were analyzed using ImageJ. Tumor cell GFP/Clover signal was separated from the spectrally overlapping myeloid CFP signal by subtraction. The isolated tumor cell borders were then automatically outlined by intensity thresholding. Analysis and extraction of outlines was performed using ROI_Tracker, a custom written plugin for ImageJ.[24] Cell protrusiveness and area along with centroid displacement and instantaneous speed were extracted and statistical analyses were performed in Graphpad Prism.

Cell protrusiveness is quantified by calculating for each time point the difference between the cell area and the cell area measured in the first time point. The standard deviation of this differential area gives the degree to which these protrusions fluctuate over time.

Quantification of the cell area was chosen over perimeter because it offers the greatest power to distinguish changes in protrusiveness. While a detailed comparison of the methods is beyond the scope of this paper, the advantage of area can be understood by considering a hypothetical geometry and examining the ratio of the fractional change for each metric (i.e. change in area divided by change in perimeter). If the ratio of these 2 fractional changes is greater than 1, then area is a better measure, if less than 1, perimeter is the better measure.

Consider a protrusion that is rectangular in shape (this is of course an approximation, but it reflects protrusions captured at a high enough frame rate well, the math is simple and it illustrates the advantage common to more complex geometries) with width W and length L. The area is A = L*W and the perimeter is P = 2*L+W (one width side is attached to the main body of the cell). The fractional change in area due to a small extension in length would be dA/A = dL * W / (L * W). For the perimeter, the percent change would be dP/P = 2*dL/(2*L+W). The ratio of these is 1+W/2L. Since this is greater than 1 for all geometries, the area is more sensitive to protrusions than is perimeter.

Blood serum exclusion was quantified in ImageJ by placing an ~80 μm ROI on each of the locations indicated in **Figure 3A** and analyzing the fluorescence signal in the dextran (Red) channel.

Supplemental Material

Supplemental data for this article can be accessed on the publisher's website

Author Contributions

DE designed the window, fixturing plate and the vacuum set up; developed and implemented the microscope optimizations; developed and performed the intubation method; performed the imaging; developed the image processing and image analysis and developed the blood averaging technique. CRT performed the analysis for the blood vessel diameter histogram. DE and JC devised amplifier optimization experiments. YK and CRT made the cell lines. YK and CRT cultured the cells and performed the experimental metastasis injections. YK, TK, and DE developed the surgical technique. YK, TK, DE, and CRT performed the surgeries. YK, CRT, DE, JWP, and JC designed the experiments and wrote the paper.

References

1. Mehlen P, Puisieux A. Metastasis: a question of life or death. Nat Rev Cancer 2006; 6:449-58; PMID:16723991; http://dx.doi.org/10.1038/nrc1886

2. Guth U, Magaton I, Huang DJ, Fisher R, Schötzau A, Vetter M. Primary and secondary distant metastatic breast cancer: two sides of the same coin. Breast 2014; 23:26-32; PMID:24215983; http://dx.doi.org/10.1016/j.breast.2013.10.007

3. Chambers AF, Groom AC, MacDonald IC. Dissemination and growth of cancer cells in metastatic sites. Nat Rev Cancer 2002; 2:563-72; PMID:12154349; http://dx.doi.org/10.1038/nrc865

4. Young J. Malpighi's "De Pulmonibus." Proc R Soc Med 1929; 23:1-11; PMID:19987199

5. Gligorijevic B, Bergman A, Condeelis J. Multiparametric classification links tumor microenvironments with tumor cell phenotype. PLoS Biol 2014; 12:e1001995; PMID:25386698; http://dx.doi.org/10.1371/journal.pbio.1001995

6. Patsialou A, Bravo-Cordero JJ, Wang Y, Entenberg D, Liu H, Clarke M, Condeelis JS. Intravital multiphoton imaging reveals multicellular streaming as a crucial component of in vivo cell migration in human breast tumors. Intravital 2013; 2:e25294; PMID:25013744; http://dx.doi.org/10.4161/intv.25294

7. Qian B, Deng Y, Im JH, Muschel RJ, Zou Y, Li J, Lang RA, Pollard JW. A distinct macrophage population mediates metastatic breast cancer cell extravasation, establishment and growth. PLoS One 2009; 4:e6562; PMID:19668347; http://dx.doi.org/10.1371/journal.pone.0006562

8. Qian BZ, Li J, Zhang H, Kitamura T, Zhang J, Campion LR, Kaiser EA, Snyder LA, Pollard JW. CCL2 recruits inflammatory monocytes to facilitate breast-tumour metastasis. Nature 2011; 475:222-5; PMID:21654748; http://dx.doi.org/10.1038/nature10138

9. Wearn JT, Barr J, German W. The Behavior of the Arterioles and Capillaries of the Lung. Exp Biol Med 1926; 24:114-5; http://dx.doi.org/10.3181/00379727-24-3250

10. Terry RJ. A Thoracic Window for Observation of the Lung in a Living Animal. Science 1939; 90:43-4; PMID:17798138; http://dx.doi.org/10.1126/science.90.2324.43

11. De Alva WE, Rainer WG. A method of high speed in vivo pulmonary microcinematography under physiologic conditions. Angiology 1963; 14:160-4; PMID:14025662; http://dx.doi.org/10.1177/000331976301400402

12. Wagner WW, Jr, Filley GF. Microscopic observation of the lung in vivo. Vasc Dis 1965; 2:229-241; PMID:5866200

13. Wagner WW, Jr. Pulmonary microcirculatory observations in vivo under physiological conditions. J Appl Physiol 1969; 26:375-7; PMID:5773180

14. Groh J, Kuhnle GE, Kuebler WM, Goetz AE. An experimental model for simultaneous quantitative analysis of pulmonary micro- and macrocirculation during unilateral hypoxia in vivo. Res Exp Med 1992; 192:431-41; http://dx.doi.org/10.1007/BF02576301

15. Fingar VH, Taber SW, Wieman TJ. A new model for the study of pulmonary microcirculation: determination of pulmonary edema in rats. J Surg Res 1994; 57:385-93; PMID:8072287; http://dx.doi.org/10.1006/jsre.1994.1159

16. Lamm WJ, Bernard SL, Wagner WW Jr, Glenny RW. Intravital microscopic observations of 15-micron microspheres lodging in the pulmonary microcirculation. J Appl Physiol 2005; 98:2242-8; PMID:15705726; http://dx.doi.org/10.1152/japplphysiol.01199.2004

17. Tabuchi A, Mertens M, Kuppe H, Pries AR, Kuebler WM. Intravital microscopy of the murine pulmonary microcirculation. J Appl Physiol 2008; 104:338-46; PMID:18006870; http://dx.doi.org/10.1152/japplphysiol.00348.2007

18. Looney MR, Thornton EE, Sen D, Lamm WJ, Glenny RW, Krummel MF. Stabilized imaging of immune surveillance in the mouse lung. Nat. Methods 2011; 8:91-6; PMID:21151136; http://dx.doi.org/10.1038/nmeth.1543

19. Presson RG Jr, Brown MB, Fisher AJ, Sandoval RM, Dunn KW, Lorenz KS, Delp EJ, Salama P, Molitoris BA, Petrache I. Two-photon imaging within the murine thorax without respiratory and cardiac motion artifact. Am J Pathol 2011; 179:75-82; PMID:21703395; http://dx.doi.org/10.1016/j.ajpath.2011.03.048

20. Vinegoni C, Lee S, Gorbatov R, Weissleder R. Motion compensation using a suctioning stabilizer for intravital microscopy. Intravital 2012; 1:115-21; PMID:24086796; http://dx.doi.org/10.4161/intv.23017

21. Patsialou A, Wang Y, Pignatelli J, Chen X, Entenberg D, Oktay M, Condeelis JS. Autocrine CSF1R signaling mediates switching between invasion and proliferation downstream of TGFbeta in claudin-low breast tumor cells. Oncogene 2014; 34(21):2721-31

22. Helmchen F, Denk W. Deep tissue two-photon microscopy. Nat. Methods 2005; 2:932-40; PMID:16299478; http://dx.doi.org/10.1038/nmeth818

23. Denk W, Strickler JH, Webb WW. Two-photon laser scanning fluorescence microscopy. Science 1990; 248:73-6; PMID:2321027; http://dx.doi.org/10.1126/science.2321027

24. Entenberg D, Wyckoff J, Gligorijevic B, Roussos ET, Verkhusha VV, Pollard JW, Condeelis J. Setup and use of a two-laser multiphoton microscope for multichannel intravital fluorescence imaging. Nat Protoc 2011; 6:1500-20; PMID:21959234; http://dx.doi.org/10.1038/nprot.2011.376

25. Fork RL, Martinez OE, Gordon JP. Negative dispersion using pairs of prisms. Opt Lett 1984; 9:150-2; PMID:19721526; http://dx.doi.org/10.1364/OL.9.000150

26. Wright A. Amplifiers for use with photomultipliers—who needs them? Nuclear Instruments and Methods in Physics Research Section A: Accelerators, Spectrometers, Detectors and Associated Equipment 2003; 504:245-9; http://dx.doi.org/10.1016/S0168-9002(03)00800-3

27. Graeme JG. Photodiode amplifiers: op amp solutions. (McGraw Hill, 1996, 31-6).

28. Ovchinnikov DA, van Zuylen WJ, DeBats CE, Alexander KA, Kellie S, Hume DA. Expression of Gal4-dependent transgenes in cells of the mononuclear phagocyte system labeled with enhanced cyan fluorescent protein using Csf1r-Gal4VP16/UAS-ECFP double-transgenic mice. J Leukoc Biol 2008; 83:430-3; PMID:17971498; http://dx.doi.org/10.1189/jlb.0807585

29. Lam AJ, St-Pierre F, Gong Y, Marshall JD, Cranfill PJ, Baird MA, McKeown MR, Wiedenmann J, Davidson MW, Schnitzer MJ, et al. Improving FRET dynamic range with bright green and red fluorescent proteins. Nat Methods 2012; 9:1005-12; PMID:22961245; http://dx.doi.org/10.1038/nmeth.2171

30. Lelkes E, Headley MB, Thornton EE, Looney MR, Krummel MF. The spatiotemporal cellular dynamics of lung immunity. Trends Immunol 2014; 35:379-86; PMID:24974157; http://dx.doi.org/10.1016/j.it.2014.05.005

31. Cameron MD, Schmidt EE, Kerkvliet N, Nadkarni KV, Morris VL, Groom AC, Chambers AF, MacDonald IC. Temporal progression of metastasis in lung: cell survival, dormancy, and location dependence of metastatic inefficiency. Cancer Res 2000; 60:2541-6; PMID:10811137

32. Morris VL, MacDonald IC, Koop S, Schmidt EE, Chambers AF, Groom AC. Early interactions of cancer cells with the microvasculature in mouse liver and muscle during hematogenous metastasis: videomicroscopic analysis.

Clin Exp Metastasis 1993; 11:377-90; PMID:8375113; http://dx.doi.org/10.1007/BF00132981

33. Scherbarth S, Orr FW. Intravital videomicroscopic evidence for regulation of metastasis by the hepatic microvasculature: effects of interleukin-1alpha on metastasis and the location of B16F1 melanoma cell arrest. Cancer Res 1997; 57:4105-10; PMID:9307300

34. Al-Mehdi AB, Tozawa K, Fisher AB, Shientag L, Lee A, Muschel RJ. Intravascular origin of metastasis from the proliferation of endothelium-attached tumor cells: a new model for metastasis. Nat Med 2000; 6:100-2; PMID:10613833; http://dx.doi.org/10.1038/71429

35. Wong CW, Song C, Grimes MM, Fu W, Dewhirst MW, Muschel RJ, Al-Mehdi AB. Intravascular location of breast cancer cells after spontaneous metastasis to the lung. Am J Pathol 2002; 161:749-53; PMID:12213701; http://dx.doi.org/10.1016/S0002-9440(10)64233-2

36. Gligorijevic B, Wyckoff J, Yamaguchi H, Wang Y, Roussos ET, Condeelis J. N-WASP-mediated invadopodium formation is involved in intravasation and lung metastasis of mammary tumors. J Cell Sci 2012; 125:724-34; PMID:22389406; http://dx.doi.org/10.1242/jcs.092726

37. Roh-Johnson M, Bravo-Cordero JJ, Patsialou A, Sharma VP, Guo P, Liu H, Hodgson L, Condeelis J. Macrophage contact induces RhoA GTPase signaling to trigger tumor cell intravasation. Oncogene 2014; 33:4203-12; PMID:24056963; http://dx.doi.org/10.1038/onc.2013.377

38. Schneider CA, Rasband WS, Eliceiri KW. NIH Image to ImageJ: 25 years of image analysis. Nat. Methods 2012; 9:671-5; PMID:22930834; http://dx.doi.org/10.1038/nmeth.2089

39. Cole RW, Jinadasa T, Brown CM. Measuring and interpreting point spread functions to determine confocal microscope resolution and ensure quality control. Nat Protoc 2011; 6:1929-41; PMID:22082987; http://dx.doi.org/10.1038/nprot.2011.407

40. Zipfel WR, Williams RM, Webb WW. Nonlinear magic: multiphoton microscopy in the biosciences. Nat Biotechnol 2003; 21:1369-77; PMID:14595365; http://dx.doi.org/10.1038/nbt899

41. Thevenaz P, Ruttimann UE, Unser MA. pyramid approach to subpixel registration based on intensity. IEEE Trans Image Process 1998; 7:27-41; PMID:18267377; http://dx.doi.org/10.1109/83.650848

42. Ewens A, Mihich E, Ehrke MJ. Distant metastasis from subcutaneously grown E0771 medullary breast adenocarcinoma. Anticancer Res 2005; 25:3905-15; PMID:16312045

43. Kitamura T, Qian BZ, Soong D, Cassetta L, Noy R, Sugano G, Kato Y, Li J, Pollard JW. CCL2-induced chemokine cascade promotes breast cancer metastasis by enhancing retention of metastasis-associated macrophages. J Exp Med 2015; 212 (7):1043-59; PMID: 26056232; PMCID: PMC4493415.